

HEAT TRANSFER BOUNDARY CONDITIONS FOR THE NUMERICAL SIMULATION OF THE DC CASTING PROCESS

Adrian Sabau¹, Kazunori Kuwana², Srinath Viswanathan³, Kozo Saito², and Lee Davis⁴

¹Oak Ridge National Laboratory; Metals and Ceramics Division; P.O. Box 2008; Oak Ridge, TN 37831-6083

²University of Kentucky; Dept. of Mechanical Engineering; 513 CRMS Bldg; Lexington, KY 40506-0108

³Sandia National Laboratories; P.O. Box 5800; Albuquerque, NM 87185-1134

⁴Wagstaff, Inc.; 3910 North Flora Road, Spokane, WA 99216

Keywords: Aluminum, DC Casting, Heat Transfer, Boundary Conditions, Simulation

Abstract

The temperature evolution during the start-up phase of the Direct Chill (DC) casting process is critical to the prediction of strain-stress evolution during solidification. The start-up phase of DC casting is complex, as heat is extracted by the mold, bottom block, and cooling water, while process parameters are ramped up to their steady state values. The modeling of DC casting involves making assumptions on the various heat transfer mechanisms, such as (a) direct contact of liquid metal and mold, (b) air gap between mold and ingot surface, (c) water cooling on rolling and end faces of the ingot, (d) ingot contact with the bottom block, and (e) water intrusion between the bottom block and ingot. The boundary conditions for the heat transfer analysis during the startup are discussed in detail. Numerical simulation results are presented for a typical casting run, including variable casting speed, metal head, and water flow rate.

Introduction

The thermal field is crucial to the prediction of state of strain and stress and subsequent cracking. Consequently, an important step in the modeling of the DC casting process involves assumptions on different heat transfer mechanisms. Heat transfer during the start-up phase of the DC casting process is complex and transient since ingot cooling is affected by: direct contact with the mold, air gap that forms in the mold, water film on rolling and end faces, direct contact with the bottom block, and water intruded between the bottom block and ingot. These cooling regimes are dealt with by prescribing heat transfer boundary conditions in the form of either heat fluxes or heat transfer coefficients. In this paper, we deal with heat transfer coefficients and heat flux boundary conditions due to water film cooling on ingot faces and in water intrusion regions between the bottom block and the ingot.

Hannart et al. (1994) used temperature and water flow rate dependent heat transfer coefficients, citing Weckman and Niessen (1984), without giving any details of their approach. Maenner et al. (1997) reviewed published data on heat transfer coefficients due to water film cooling. They pointed out that at high temperatures the literature data has a large scatter. Chang and Kang (1999) presented results for the heat flux as a function of temperature. Their results were reported for flow rates that correspond to two holes/in. and four holes/in., respectively, along the edge of the mold. Du et al. (1998) used temperature and water flow rate dependent heat transfer coefficients. In some recent studies, such as that by Drezet et al. (2000), the

dependence of the heat transfer coefficient on the water flow rate is not mentioned. Droste et al., (2000) indicate that the heat transfer coefficient due to water film cooling will be altered as a function of the water flow rate, but the proposed reduction function is not given. Grealy et al. (2001) presented an approach to account for the change in the Leidenfrost temperature point with water flow rates. Sengupta et al. (2003) accounted for water film ejection, which can occur at low flow rates. It is only recently that water intrusion was considered in studies such as those by Droste et al., (2000) and Sengupta et al. (2003).

As part of a project on reducing ingot cracking in the DC casting process, our team performed some experiments at Wagstaff, Inc. During these experiments the following physical phenomena were observed: (a) End faces are cooled faster than the rolling faces due to their higher water flow rates than on rolling faces, (b) Water flow and ensuing cooling in corner regions is different than those on ingot faces since water flow holes near the corner were closed to insure proper cooling in corner regions, and (c) Water intrusion occurs in a different manner at the rolling face than on the end face. Some of these phenomena were not reported in previous studies. In this paper, the occurrence of these phenomena is documented and approaches to account for these phenomena are presented.

Numerical Simulation of the DC Casting Process

A mathematical model of the DC casting process was developed using the commercial code ProCAST by employing several assumptions that simplify the physical system. The time evolution of casting parameters was determined from the casting recipe (casting speed, metal height, and water flow rate versus cast length) provided by Wagstaff, Inc. Geometry data was obtained for the mold and bottom block from Wagstaff, Inc. (Figure 1).

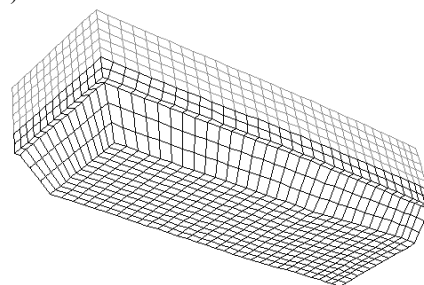


Figure 1. Geometry for the ingot mesh (black-initial liquid metal; gray-additional layers).

In ABAQUS, the ingot growth can be handled by adding layers of new material elements since the Navier-Stokes equations for fluid flow were not solved. Boundary conditions for heat transfer and deformation analysis were handled by continuously adding layers of elements at the top surface of ingot. In ABAQUS, heat transfer boundary conditions in water intrusion regions can be easily imposed using user subroutines. In ProCAST, the fluid flow as well as solid deformation were considered. However, no framework was yet available in ProCAST for handling the water intrusion regions.

Primary Cooling

The heat transfer coefficient with the mold was assumed to be 2000 W/m²K for mold contact, and 200 W/m²K in the air gap regions. A sink temperature of 100°C was assumed in both cases. Following Droste et al. (2000), the air gap was assumed to be spread over approximately half of the ingot area that overlaps with the mold. The heat transfer coefficient with the bottom block was obtained from Mortensen (1999).

Water Film Cooling

The reference data for the heat transfer coefficient for water film cooling is that from Drezet et al., 2000. Drezet et al. (2000) determined the heat transfer coefficient based on an inverse heat transfer analysis for the case in which the water flow rate was 2.63 l/min/cm. In this study, those values for the heat transfer coefficient were adjusted in order to account for the actual water flow rate. The casting recipe includes a large variation between the start-up flow rate and that corresponding to the steady-state regime.

Water Flow Distribution on Ingot Faces

The water flow rates on the rolling and end faces of the ingot were different since different hole spacings were used in the mold faces corresponding to the rolling and end faces of the ingot. The water flow rate per unit length for each face was computed based on the number of holes per unit length as shown in Table 1.

Table 1. Flow rate at start-up and steady-state regimes computed based on number of holes per unit length.

DC regime	Ingot Face	Water flow rate [l/min]	W , Water flow rate l/min/cm	Water flow rate l/min/face
Start-up	Rolling	225	0.4	32.78
	End	225	0.54	79.74
Steady-state	Rolling	760	1.35	110.72
	End	760	1.82	269.34

Dependence of Water Film Cooling on the Water Flow Rate

A power-law formulation derived by Weckman and Niessen (1982) is used in many studies to relate the heat flux on the ingot surface to the water flow. Chang and Kang (1999) presented results for the heat flux as a function of temperature. Their results were reported for flow rates that correspond to two holes/inch (0.8 hole/cm) and four holes/inch (1.6 hole/cm), respectively. When the water flow rate increases by a factor of two, the maximum heat flux increases by half. In this study, we

assume that the maximum heat transfer coefficient at a given water flow rate, W , is directly proportional to heat transfer coefficient, h_{\max}^0 , at the reference water flow rate, W_0 , i.e.,:

$$h_{\max}(W, W_0) = f_{FR}(W, W_0) h_{\max}^0 \quad (1)$$

where f_{FR} is the flow rate factor based on the maximum heat transfer coefficient. If the maximum heat flux is considered to depend linearly on the water flow rate, based on the experimental data of Chang and Kang (1999), the water flow rate factor can be determined as:

$$f_{FR}(W, W_0) = 0.5 \left(1 + \frac{W}{W_0} \right) \quad (2)$$

Results presented by Grealy et al. (2001), indicate that for $W_0=1.1$ l/min cm and $W=2.2$ l/min cm, $f_{FR}=1.14$, while the estimate using Equation 2, which is based on the Chang and Kang (1999) data, yields a value of $f_{FR}=1.5$. This value of 1.5 is also supported by the results presented by Grandfield et al. (1997) for the case in which the water flow rate was varied from 20 l/min to 40 l/min. The increase in the flow rate has an effect on the onset of the nucleate boiling temperature and on the Leidenfrost temperature point (Grealy et al., 2001). Let us consider that the Leidenfrost temperature varies with the flow rate as follows:

$$T_{LD}(W, W_0) = T_{LD}^0 + \Delta T_{LT}(W, W_0) \quad (3)$$

By considering a linear dependence on the Leidenfrost temperature shift factor, ΔT_{LT} , on the water flow rate, the following expression can be obtained based on the results presented by Grealy et al. (2001):

$$\Delta T_{LT}(W, W_0) = 15.0 \left(\frac{W}{W_0} - 1 \right) \quad (4)$$

For this study, the heat transfer coefficient (HTC) was computed by taking into account (a) the flow rate variation in time, (b) the flow rate distribution on the rolling and end faces, (c) the heat transfer coefficient variation with the flow rate, and (d) the variation of Leidenfrost temperature with the flow rate. The HTC was computed using the actual water flow rates [l/min/cm] for each of the rolling faces, W_R , and end faces, W_E (Table 1). For the case when $W_0=2.63$ l/min/cm, the predicted values for the heat transfer coefficient are shown in Tables 2 and 3 for the rolling face and end face of the ingot, respectively.

Heat Transfer Boundary Conditions at the Ingot Corners

The heat transfer at the corners is different from that at the end faces as a certain number of holes near the ingot corner were closed in order to provide appropriate cooling conditions at the corner (Figure 2). In the configuration considered, four water holes were closed on the rolling faces and end faces of the ingot.

Experimental observations indicate that the water spreads in the corner regions such that after a certain distance along the ingot length, the two water streams come in contact with each other (Figure 3). In this work, the angle at which the streams deviate from the vertical direction is considered to be equal to 30°. This phenomenon is shown schematically in Figure 3. For each element face in the corner region, the HTC is taken to be a fraction of the computed HTC for water film cooling corresponding to the respective ingot face.

Table 2. Heat transfer coefficient on the rolling face, $h_w^R = h_w(T, W_R, W_0)$ [W/m²K], for $W_0=2.63$ l/min/cm.

W=225 l/min		W=320 l/min		W=500 l/min		W=670 l/min		W=760 l/min	
T [°C]	HTC								
25	5000	25	5000	25	5000	25	5000	25	5000
70	5000	70	5000	70	5000	70	5000	70	5000
80	8000	80	8000	80	8000	80	8000	80	8000
120	28802	120	34889	120	46304	120	57337	120	63044
267	4610	274	5584	286	7411	297	9177	303	10091
367	771	374	934	386	1240	397	1535	403	1688
800	771	800	771	800	771	800	771	800	771

Table 3. Heat transfer coefficient on the end face of the ingot, $h_w^E = h_w(T, W_E, W_0)$ [W/m²K], for $W_0=2.63$ l/min/cm.

W=225 l/min		W=320 l/min		W=500 l/min		W=670 l/min		W=760 l/min	
T [°C]	HTC								
25	5000	25	5000	25	5000	25	5000	25	5000
70	5000	70	5000	70	5000	70	5000	70	5000
80	8000	80	8000	80	8000	80	8000	80	8000
120	33842	120	42060	120	57470	120	72365	120	80070
273	5417	281	6732	297	9198	313	11583	321	12816
373	906	381	1126	397	1538	413	1937	421	2143
800	771	800	771	800	771	800	771	800	771



Figure 2. Water flow near a corner of the mold.

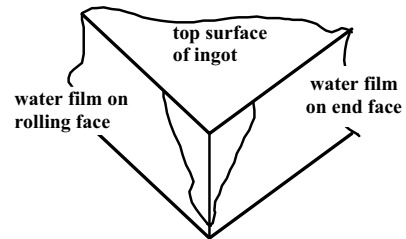


Figure 3. Water flow pattern near a corner of the ingot.

The “corner” fraction was considered to be 20%. More investigations are required to determine more accurate heat transfer boundary conditions for the corner regions. In summary, the regions on ingot faces, where various heat transfer mechanisms are dominant, are sketched in Figure 4. These regions are: direct contact with the mold, air gap between the mold and ingot, water cooled regions on rolling faces, end faces, and ingot corners.

Water Intrusion

Holes are drilled in the bottom block near the end face of the ingot in order to drain the water that gets in the gap formed between the ingot and bottom block due to butt curl (Figure 5). The evolution of the water intrusion between the bottom block and the ingot was determined based on experimental observations and the temperature distribution in the bottom block. A large amount of water intrudes through the end faces of the ingot (see Figure 6) and a small amount of water intrudes on the rolling face (see Figure 7). On the rolling face, the amount of water intrusion increases from its center towards the corner.

In order to identify the onset of water intrusion, temperature data obtained at locations in the bottom block and ingot [Figure 8(a)], were analyzed.

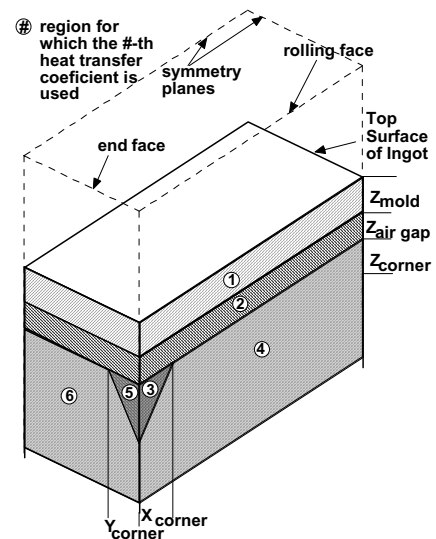


Figure 4. Regions of various heat transfer mechanisms on ingot faces. Numbers indicate the different regions.

On the rolling face, the amount of water intrusion increases from its center towards the corner.

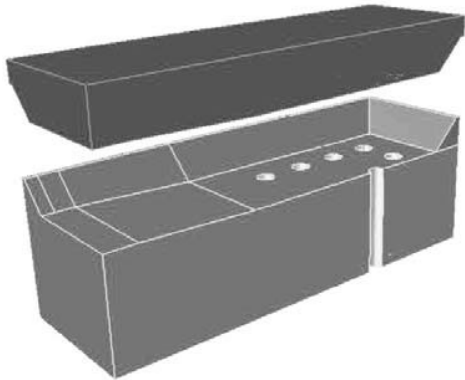


Figure 5. Liquid metal (top) when the bottom block withdrawal starts and bottom block (bottom) with drain holes.



Figure 6. Water intrusion near the corner region showing that water intrudes mainly from the end face.



Figure 7. Water intrusion on the rolling face.

In order to identify the onset of water intrusion, temperature data obtained at locations in the bottom block and ingot [Figure 8(a)], were analyzed. The progression of the water intrusion was inferred from the sharp temperature shifts in the thermocouple data. The temperature shifts are clearly due to the onset of additional cooling, which in those regions could only be due to water intrusion. The times of the temperature shifts are shown in Figure 8(b). The contact area between the ingot and bottom block was divided into several regions based on how the water intrusion evolves in time [see Figure 9].

Based on the thermocouple data and experimental observations of the water intrusion, the following features were observed:

- Water intrusion starts along the inclined edges of the bottom block and ingot, i.e., surfaces A and B (Figure 9(b)).
- The water intrusion front propagates from the end faces toward the center of the ingot.

- More water was found to intrude from the end faces than from the rolling faces due to a larger gap between the ingot and the bottom block at the end faces.

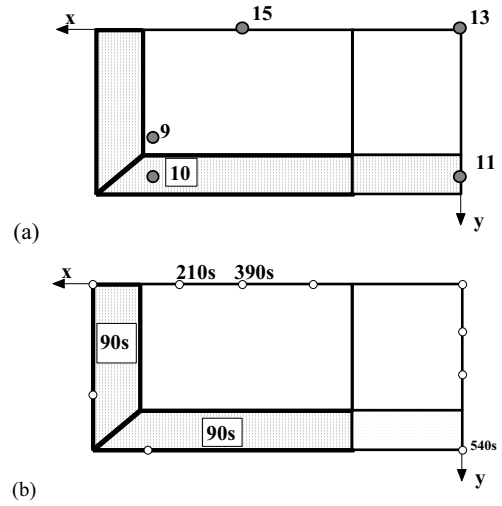


Figure 8. (a) Thermocouple placement, (b) time at which water intrusion starts at specific locations.

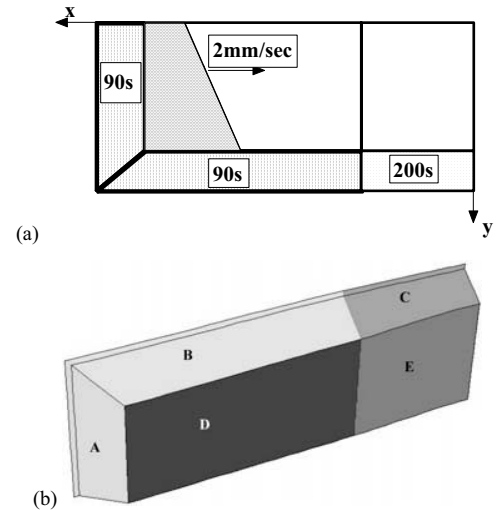


Figure 9. Water intrusion: (a) onset and evolution of the water intrusion front based on experimental data and (b) sketch of different water intrusion regions.

Heat Transfer Coefficient at Water Intrusion Regions

In the water intrusion regions, the ingot and bottom block are in contact with a mixture of water, water vapor, and air. The heat flux per unit area was computed based on a weighted area average of the heat fluxes due to water and air using the following relationship:

$$q_{\text{int}}'' = f_{wc} h_w(T, W_{\text{int}}, W_o)(T - T_{sw}) + (1 - f_{wc}) h_a(T)(T - T_{sa}), \quad (5)$$

where f_{wc} is the fractional area in contact with water, $h_w(T, W_{\text{int}}, W_o)$ is the heat transfer coefficient corresponding to the water intrusion flow rate, W_{int} , at the surface temperature T ,

T_{sw} is the sink temperature used to compute the water heat flux, and $h_a(T)$ is the heat transfer coefficient at the surface temperature T . T_{sa} is the sink temperature used to compute the air heat flux. For the case in which the sink temperatures are taken to be the same, i.e., $T_{sw} = T_{sa} = T_s$, the heat transfer coefficient in water intrusion areas becomes:

$$h_{w,i}(T, W_{int}, W_o) = f_{wc} h_w(T, W_{int}, W_o) + (1 - f_{wc}) h_a(T). \quad (6)$$

It is now assumed that the intruding water flow rate is a fraction, f_w , of the water flow rate on the rolling face, W_R , or end face, W_E , respectively:

$$W_{int}(t) = \begin{cases} f_w W_R(t) & \text{water intrusion close to rolling faces,} \\ f_w W_E(t) & \text{water intrusion close to end faces.} \end{cases} \quad (7)$$

At the bottom surface [i.e., surfaces D and E (Figure 9)], it is assumed that the water intrudes from both the end and rolling faces. As a first approximation, it is assumed that the heat transfer coefficient is the average between the heat transfer coefficient due to water intrusion from the rolling face, $h_{w,i}^R$, and that from the rolling faces, $h_{w,i}^E$:

$$h_{w,i}^B = f_{WE} h_{w,i}^E(T, W_{int}^E, W_o) + (1 - f_{WE}) h_{w,i}^R(T, W_{int}^R, W_o) \quad (8)$$

In this study, $f_{wc} = 0.3$, $f_w = 0.3$, $f_{WE} = 0.8$, and $T_s = 25.0$.

For the region on the bottom surface without drain holes, i.e., in the center of the ingot, only water from the rolling faces is considered to intrude.

Numerical Simulation Results

In this section, numerical simulation results are shown for two cases (Table 4). In the first case, i.e., labeled “ne-nc”, the same heat transfer coefficient $h_w(T, W_R, W_o)$ was used on the entire ingot surface, irrespective of the water flow rate on the end face or the water flow pattern near the corner regions. In the second case, labeled, “e-c” both end face effects and corner effects are considered. The numerical simulations were performed using ProCAST software.

Table 4. Cases considered for numerical simulation.

Case notation	HTC on end face, h_w^E	Corner	Water intrusion
ne-nc	Same as on rolling face, i.e., $h_w(T, W_R, W_o)$	No	No
e-c	Different than on rolling face, i.e., $h_w(T, W_E, W_o)$	Yes	No

In order to assess the effect of using more appropriate HTCs for the end face and corner regions, data on solidification and temperature evolution were obtained for the two cases considered at selected points located on the end face. The selected points are located at the intersection of the dashed lines shown in Figure 10 and their position is given by the respective Y and Z coordinates. In Figures 11(a) and (b), the solid fraction evolution is shown for points situated at a height of 5 and 29 cm, respectively. At Z=5 cm, solidification proceeds almost identically in both cases as these points are located initially in the mold region. As the ingot is withdrawn, the air gap forms and remelting is observed at those locations. At times greater than 150s, water cooling commences and the solidification

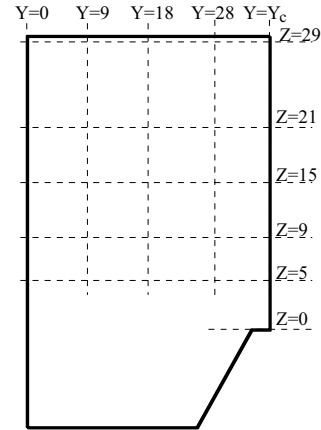


Figure 10. Points selected on the end face for showing numerical simulation results.

curves start to slightly diverge, showing the effect of using different HTC on the end face for the two simulation cases considered. This effect is more evident at locations where Z=29 [Figure 11(b)]. The temperature evolution is shown in Figure 12(a-c) for points at Z=5 and 29 cm. For the sake of clarity, two figures [12(a) and (b)] are used for temperature results at Z=5 cm. The temperature difference for the two cases is significantly greater in Figure 12(b) owing to the use of larger HTCs for higher water flow rates on the end face than those for the rolling face. The difference between the temperatures for the two different cases increases from the center at the ingot (Y=0) to the corner (Y=Yc). At the location of Z=29 cm, the temperature evolution [Figure 12(c)] does not show a significant difference even though the solid fraction shows a difference [Figures 11(a) and (b)]. It is expected that the different effects observed in temperature and solid fraction between the two cases considered will also result in the differences between the state of stress and deformation of the ingot.

Conclusions

Appropriate heat transfer boundary conditions must be applied on various regions on the ingot surface according to the different heat transfer mechanisms that take place. Based on experimental observations of a DC casting run, the following physical phenomena were discussed: end faces cooled faster than the rolling faces due to their higher water flow rates than on rolling faces, water flow and ensuing cooling in corner regions was different than those on ingot faces, water intrusion occurred in a different manner at the rolling face than at the end face.

Data on solid fraction and temperature evolution were compared at points located on the end face for the two cases in which heat transfer conditions (a) were assumed to be the same on both ingot faces, and (b) were assumed to be different on the two ingot faces and in the corner. Small differences in solid fraction were observed while temperature distribution showed significant differences when more appropriate heat transfer boundary conditions were used on the end face and corner regions.

Acknowledgments

This work was performed for the project on Modeling and Optimization of Direct Chill Casting for Reducing Ingot

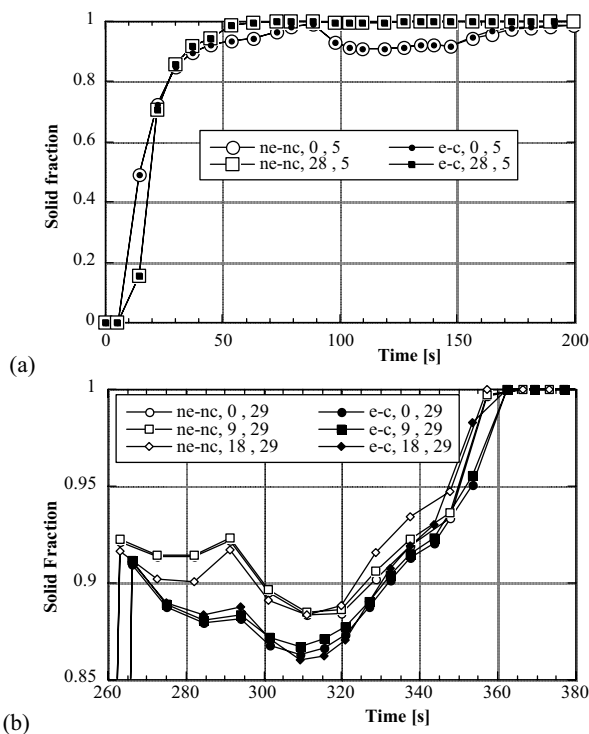


Figure 11. Evolution of fraction solid at various locations on the end face. (Legend indicates case simulation, y-location from the ingot symmetry plane, and z-location from the starting head rim as indicated in Figure 10).

Cracking in collaboration with Secat, Inc. We would like to thank the staff at Wagstaff, Inc. for allowing access to their casting facility, J. A. Clark for assistance with thermocouples, T. J. Huxford and Q. Han for reviewing the manuscript, and G. R. Carter for typing the manuscript. The research was sponsored by the U.S. Department of Energy, Assistant Secretary for Energy Efficiency and Renewable Energy, Office of Industrial Technologies, Aluminum Industries of the Future Program, under contract DE-AC05-00OR22725 with UT-Battelle, LLC. Sandia is a multiprogram laboratory operated by Sandia Corporation, a Lockheed Martin Company, for the U.S. Department of Energy's National Nuclear Security Administration under contract DE-AC04-94AL85000.

References

Drezet, Rappaz, Grun, and Gremaud, 2000, Metall. and Mater. Trans., Vol. 31A, pp. 1627-1634.
 Chang, K-M., and Kang, B., 1999, Journal of Chinese Inst. of Engineers, Vol. 22, pp. 27-42.
 Grealy, P.G., Davis, J.L., Jensen, E.K, Tondel, P.A., Moritz, J., 2001, Light Metals 2001, TMS, Warrendale, PA, pp. 813-821.
 Grandfield, J.F., Hoadley, A., Instone, S., 1997, Light Metals 1997, ed. R. Huglen, TMS, Warrendale, PA, pp. 691-699.
 Droste, W., Drezet, J-M., Gruen, G-U., Schneider, W., 2000, Eds: K. Ehrke and W. Schneider, DGM, Wiley-VCH, Frankfurt, Germany, Nov. 13-15, pp. 175-183.

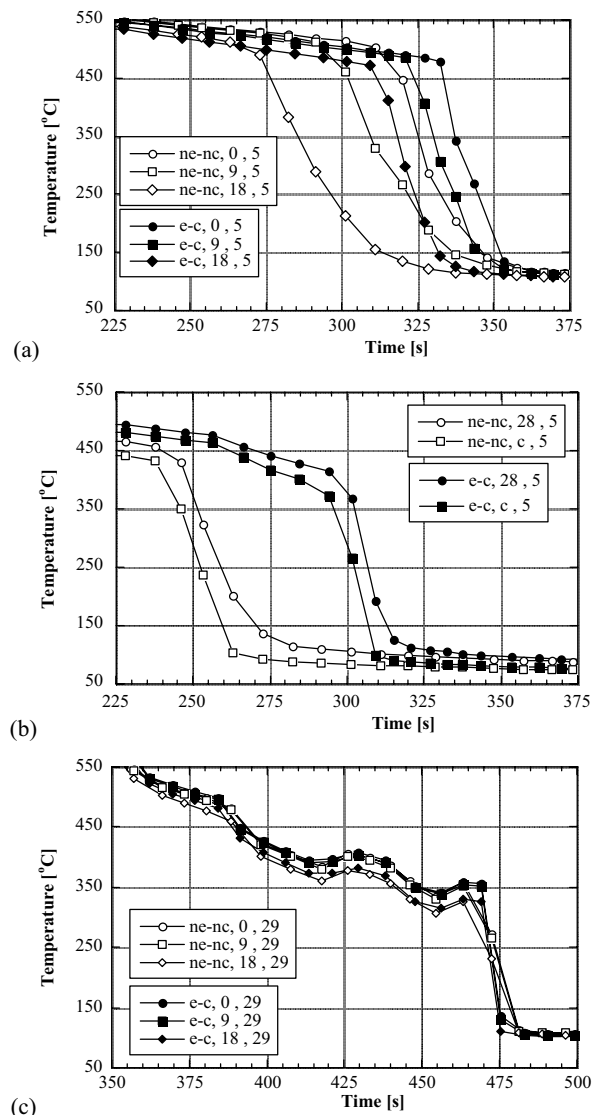


Figure 12. Evolution of temperature at various locations on the end face.

Mortensen, D., 1999, Metall. and Mater. Trans., Vol. 30B, pp. 119-133.
 Sengupta, J., Maijer, D., Wells, M.A., Cockcroft, S.L., Larouche, A., 2003, Light Metals 2003, ed. P.N. Crepeau, TMS, Warrendale, PA, pp. 841-847.
 Maenner, L. Magnin, B., Caratini, 1997, Light Metals 1997, ed. R. Huglen, TMS, Warrendale, PA, pp. 701-707.
 Hannart, B., Cialti, F., Van Schalkwijk, R., 1994, Light Metals 1994, ed. U. Mannweiler, TMS, Warrendale, PA, pp. 879-887.
 Kiss, L.I., Meenen, T., Charette, A., Lefebvre, Y., Levesque, R., 2003, Light Metals 2003, ed. P.N. Crepeau, TMS, Warrendale, PA, pp. 829-834.
 Sommerhofer, H., 2003, Light Metals 2003, ed. P.N. Crepeau, TMS, Warrendale, PA, pp. 733-740.